Front. Mech. Eng. 2022, 17(1): 9
https://doi.org/10.1007/s11465-021-0665-z

RESEARCH ARTICLE

# Mesh relationship modeling and dynamic characteristic analysis of external spur gears with gear wear

**Zhixian SHEN[a,b], Laihao YANG[a,b], Baijie QIAO (✉)[a,b], Wei LUO[a,b], Xuefeng CHEN[a,b], Ruqiang YAN[a,b]**

[a] *School of Mechanical Engineering, Xi'an Jiaotong University, Xi'an 710049, China*
[b] *State Key Laboratory for Manufacturing Systems Engineering, Xi'an Jiaotong University, Xi'an 710061, China*
✉ *Corresponding author. E-mail: qiao1224@xjtu.edu.cn (Baijie QIAO)*



**ABSTRACT** Gear wear is one of the most common gear failures, which changes the mesh relationship of normal gear. A new mesh relationship caused by gear wear affects meshing excitations, such as mesh stiffness and transmission error, and further increases vibration and noise level. This paper aims to establish the model of mesh relationship and reveal the vibration characteristics of external spur gears with gear wear. A geometric model for a new mesh relationship with gear wear is proposed, which is utilized to evaluate the influence of gear wear on mesh stiffness and unloaded static transmission error (USTE). Based on the mesh stiffness and USTE considering gear wear, a gear dynamic model is established, and the vibration characteristics of gear wear are numerically studied. Comparison with the experimental results verifies the proposed dynamic model based on the new mesh relationship. The numerical and experimental results indicate that gear wear does not change the structure of the spectrum, but it alters the amplitude of the meshing frequencies and their sidebands. Several condition indicators, such as root-mean-square, kurtosis, and first-order meshing frequency amplitude, can be regarded as important bases for judging gear wear state.

**KEYWORDS** gear wear, mesh relationship, mesh stiffness, transmission error, vibration characteristics

## 1 Introduction

Gear transmissions are widely applied in the transmission system of mechanical equipment, such as helicopter, wind turbine, and gear turbofan engine. The vibration and noise of gear transmission systems are the key indicators to determine whether the equipment is operating normally. Gear fault is one of the main factors of transmission system shutdown and failure, which is usually monitored with vibration features. The dynamic modeling and analysis of gear transmissions with typical faults, such as tooth wear, crack, and spalling, are generally utilized to acquire the feature priori of health condition motoring and fault diagnosis. Gear wear, one of the most common and typical failure modes in the early stage, usually leads to serious failure. Therefore, accurately evaluating the influence of gear wear on the vibration features of transmission systems is of great importance. This paper focuses on the dynamic modeling and vibration characteristics of external spur gears with gear wear, which could offer guidance for the fault diagnosis of gear transmission systems.

Fault modeling has been developed as the basis of dynamic modeling of gear wear. In the investigation of the calculation of gear wear on tooth profile, researchers [1–4] have proposed several models to evaluate the wear distribution of external and internal gears based on Archard's model. Thus, the results of the wear distribution obtained from these models are used to study the effect of gear wear on gear dynamics in this paper. Based on the results of wear distribution, several studies have introduced the effects of gear wear on gear ratio, tooth profile deviation, backlash, transmission error, and mesh stiffness. Gear ratio variation with tooth wear was studied in Ref. [5]. Inspired by this literature, the gear mesh relationship of gear wear is investigated in this paper. Figure 1 depicts the mesh relationship of perfect profile and worn profile. As for tooth profile deviation with tooth wear, tooth wear is directly equivalent to composite tooth profile deviation, which was introduced into gear dynamics [6]. Moreover, in Ref. [7], tooth wear was directly assumed as gear backlash and involved in the dynamic model to evaluate its influence on the dynamic

*Received July 5, 2021; accepted November 11, 2021*

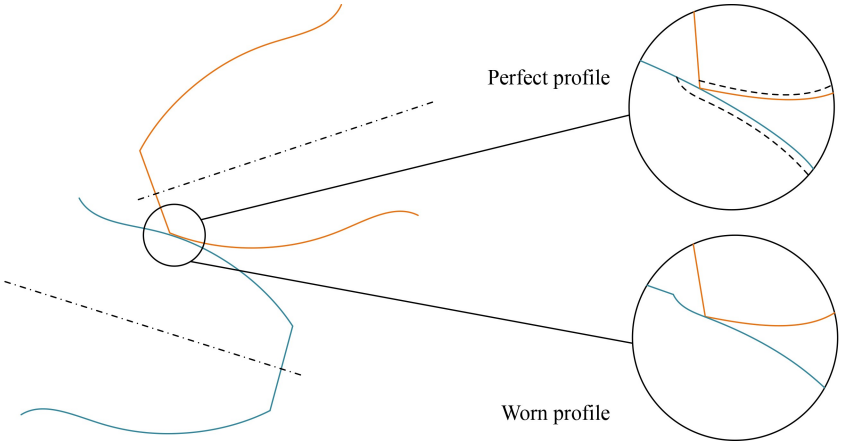


**Fig. 1** Comparison of mesh relationships between perfect profile and worn profile.

behaviors of the gear system. Transmission error with tooth wear was studied through the finite element model [8]. By assuming wear depth as profile error and considering dynamic contact load, transmission error was obtained and analyzed [9]. As for mesh stiffness with tooth wear, the influence of gear wear on the amplitude and the phase of mesh stiffness was qualitatively analyzed [10]. The reduction of mesh stiffness was measured by using modal analysis [11]. The loaded tooth contact analysis method was used to evaluate the influence of tooth wear on the mesh stiffness and the transmission error of spur gears [12,13], and this method was used in thin-rimmed gears with tooth wear [14]. The influence of tooth wear on mesh stiffness was modeled by the variation of contact lines [15]. Tooth wear was introduced into mesh stiffness with the variation of tooth profile parameters [16]. In addition, tooth wear can be regarded as a kind of tooth profile deviation, where mesh stiffness is derived through tooth deformation with gear meshing force, and two gears are regarded as rigid bodies while two meshing teeth can contact and penetrate each other [17,18]. However, state-of-the-art researchers generally utilize direct or equivalent methods to evaluate the effect of gear wear on gear meshing excitations, such as backlash, transmission error, and mesh stiffness, while the new mesh relationship caused by gear wear is neglected.

Dynamic modeling is a widely used method to obtain vibration characteristics. A dynamic wear model was proposed in gear dynamics [19], which can obtain an accurate wear depth. With the help of commercial software and contact theory, gear wear was updated by the obtained contact pressure, and then the results were introduced into the finite element model to gain dynamic responses under the influence of gear wear [20]. Transmission error was used as the indicator to assess the condition of gear wear, but no dynamic/kinematic explanation was provided [21]. The wear mechanism of vibration signal was presented, and its cyclostationary property was used to track wear condition [22,23]. In Ref. [24], measured signals were compared with the dynamic model to update the wear process. Interactions between gear dynamics and tooth wear were investigated in Refs. [12,25]. However, to the knowledge of the authors, the dynamic modeling of gear wear considering the new mesh relationship remains a critical issue that needs to be addressed.

Compared with our previous work [26,27], the mesh relationship of gear wear was not considered, and the influence of gear wear on mesh stiffness was calculated using simplified and equivalent methods. This paper focuses on the mesh relationship modeling and the dynamic characteristic analysis of external spur gears with gear wear. Specifically, a geometric model for the new mesh relationship caused by gear wear is presented and deduced analytically. Based on the proposed geometric model, mesh stiffness and transmission error are studied, which is the basis of developing an analytical dynamic model to obtain the vibration characteristics. The numerical and experimental results are compared to verify the vibration characteristics.

This paper is organized as follows. A gear geometric model is established, and the new mesh relationship with gear wear is deduced in Section 2. A gear dynamic model is established in Section 3. The vibration characteristics of gear wear are obtained in Section 4. The experimental verification is described in Section 5. Finally, the conclusions are drawn in Section 6.

## 2 New mesh relationship considering gear wear

The relative kinematic relation of meshing gears is mathematically described by the gear mesh relationship. However, the presence of gear wear often changes the complete tooth profile of two gears, which leads to the alteration of the original relative kinematic relation of meshing gears, consequently forming a new mesh relationship. First, the geometric model of a single tooth

in the driving and driven gears is established. Then, based on two geometric models, the geometric model of single-tooth meshing with gear wear is established. Thus, the new mesh relationship is deduced by solving these geometric equations.

### 2.1 Gear mesh relationship modeling

Figure 2 depicts the mesh relationship of a pair of perfect involute gears. In this figure, $O_1$ and $O_2$ are the geometric centers of two gears, $R_1$ and $R_2$ are the radii of the pitch circle, and $R_{b1}$ and $R_{b2}$ are the radii of the base circle. When a pair of gears is engaged, the meshing point moves on the ideal meshing line $N_1N_2$ with the rotation of two gears. In general, local gear failures do not change the meshing condition of spur gears, such as tooth spalling, pitting, and crack. However, gear wear changes the tooth involute profile, thus forming a new mesh relationship when two gears are engaged, that is, the meshing point is no longer on the meshing line $N_1N_2$, and a new mesh relationship needs to be deduced.

Figure 3 shows the geometric model of a single tooth in the driving gear, where $XOY$ and $X_1OY_1$ denote the fixed global coordinate system and the local coordinate system rotating with the driving gear, respectively; $A_{1\text{perfect}}$ and $A_1$ represent the meshing points on the perfect profile and the worn profile of the driving gear, respectively; $R_{A1\text{perfect}}$ and $R_{A1}$ represent the corresponding radii of the meshing points $A_{1\text{perfect}}$ and $A_1$, respectively; $\varphi_1$ depicts the rotational angle of the gear; and $h_{A1\_x1}$ depicts the wear depth in the perfect meshing point $A_{1\text{perfect}}$.

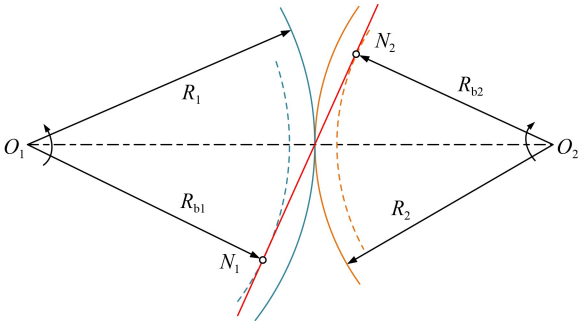


**Fig. 2** Schematic diagram of gear transmission for perfect involute external spur gears.

In the local coordinate system $X_1OY_1$, the geometric relationships of a single tooth in the driving gear are as follows:

$$\gamma_{1\text{perfect}} = \arctan(\alpha_2 + \alpha_1) - \alpha_1, \tag{1}$$

$$R_{A1\text{perfect}} = \frac{R_{b1}}{\cos\left(\alpha_1 + \gamma_{1\text{perfect}}\right)}, \tag{2}$$

$$\gamma_1 = \arctan\frac{R_{A1\text{perfect}}\sin\gamma_{1\text{perfect}} - h_{A1\_x1}}{R_{A1\text{perfect}}\cos\gamma_{1\text{perfect}}}, \tag{3}$$

$$R_{A1} = \frac{R_{A1\text{perfect}}\cos\gamma_{1\text{perfect}}}{\cos\gamma_1}, \tag{4}$$

where $\alpha_2$ and $\alpha_1$ represent the angles of the base circle and the perfect meshing point $A_{1\text{perfect}}$ on the single-tooth profile, respectively, and $\gamma_{1\text{perfect}}$ and $\gamma_1$ represent the angles of the perfect meshing point $A_{1\text{perfect}}$ and the worn meshing point $A_1$, respectively.

Correspondingly, the local coordinate system of the driven gear is $X_2O_2Y_2$ rotating with the driven gear, as shown in Fig. 4. $A_{2\text{perfect}}$ and $A_2$ represent the meshing points on the perfect profile and the worn profile of the driven gear, respectively. Correspondingly, $R_{A2\text{perfect}}$ and $R_{A2}$ represent the radii of the meshing points $A_{2\text{perfect}}$ and $A_2$, respectively, and $h_{A2\_x2}$ depicts the wear depth in the perfect meshing point $A_{2\text{perfect}}$.

Therefore, the geometric relationships of a single tooth

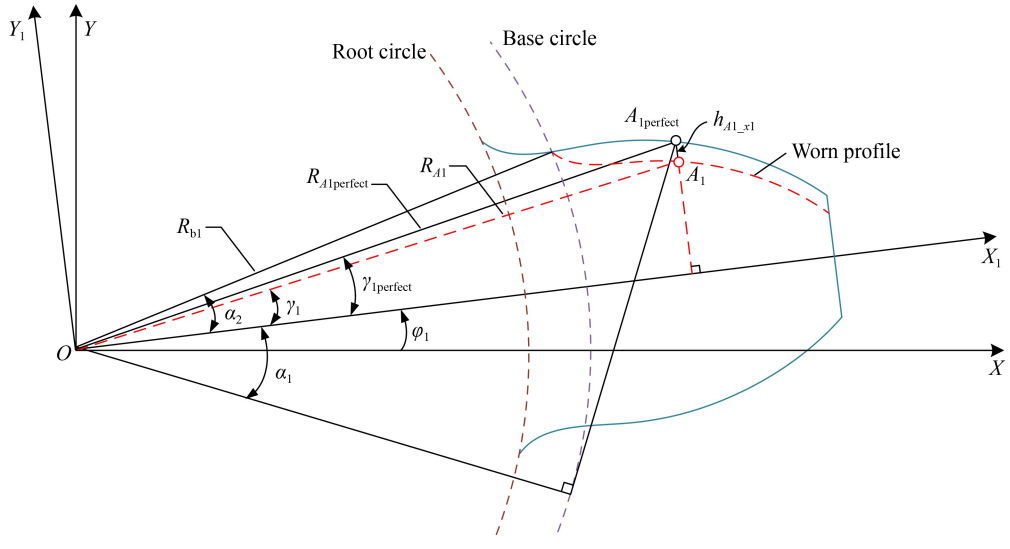


**Fig. 3** Geometric model of a single tooth in the driving gear.

in the driven gear are as follows:

$$\gamma_{2\text{perfect}} = \arctan\left(\alpha_2' + \alpha_1'\right) - \alpha', \tag{5}$$

$$R_{A2\text{perfect}} = \frac{R_{\text{b2}}}{\cos\left(\alpha_1' + \gamma_{2\text{perfect}}\right)}, \tag{6}$$

$$\gamma_2 = \arctan\frac{R_{A2\text{perfect}}\sin\gamma_{2\text{perfect}} - h_{A2\_x2}}{R_{A2\text{perfect}}\cos\gamma_{2\text{perfect}}}, \tag{7}$$

$$R_{A2} = \frac{R_{A2\text{perfect}}\cos\gamma_{2\text{perfect}}}{\cos\gamma_2}, \tag{8}$$

where $\alpha_2'$ and $\alpha_1'$ represent the angles of the base circle and the perfect meshing point $A_{2\text{perfect}}$ on the single-tooth profile, respectively, and $\gamma_{2\text{perfect}}$ and $\gamma_2$ represent the angles of the perfect meshing point $A_{2\text{perfect}}$ and the worn meshing point $A_2$, respectively.

Based on the geometric model of a single tooth, the geometric model of single-tooth meshing with gear wear is established, as shown in Fig. 5. This figure contains two meshing points, $A_1$ and $A_2$, and three coordinates, $XOY$, $X_1OY_1$, and $X_2O_2Y_2$. Through the axis $OO_2$ of two gears, the fixed global coordinate system $XOY$ is established, and each gear has a local coordinate system rotating with it, $X_1OY_1$ and $X_2O_2Y_2$, for the driving and driven gears, respectively. Additionally, $t_1$ and $t_2$ represent the tangents of two meshing points.

To deduce the new mesh relationship of worn gears, the following geometric principles should be followed:

(1) As the gear rotates, the meshing point changes from tooth root to tip for the driving gear, and opposite is true for the driven gear.

(2) The center distance of two gears $a_\omega$ remains unchanged, and the geometric expression is as follows:

$$R_{A1}\cos\left(\gamma_1 + \varphi_1\right) + R_{A2}\cos\left(\varphi_2 - \gamma_2\right) = a_\omega. \tag{9}$$

(3) When the meshing points $A_1$ and $A_2$ are engaged, the axis $Y$ of two meshing points in the coordinate system $XOY$ are the same.

$$R_{A1}\sin\left(\gamma_1 + \varphi_1\right) = R_{A2}\sin\left(\varphi_2 - \gamma_2\right). \tag{10}$$

(4) When the meshing points $A_1$ and $A_2$ are engaged, the tangents of two meshing points coincide completely.

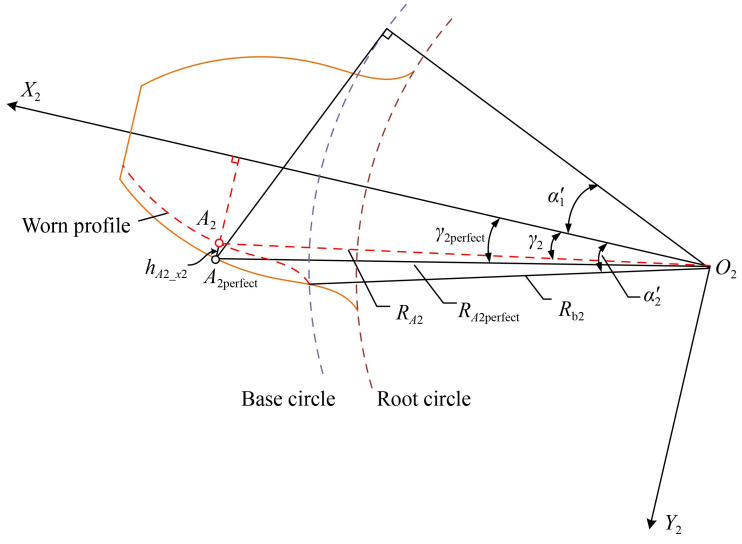


**Fig. 4** Geometric model of a single tooth in the driven gear.

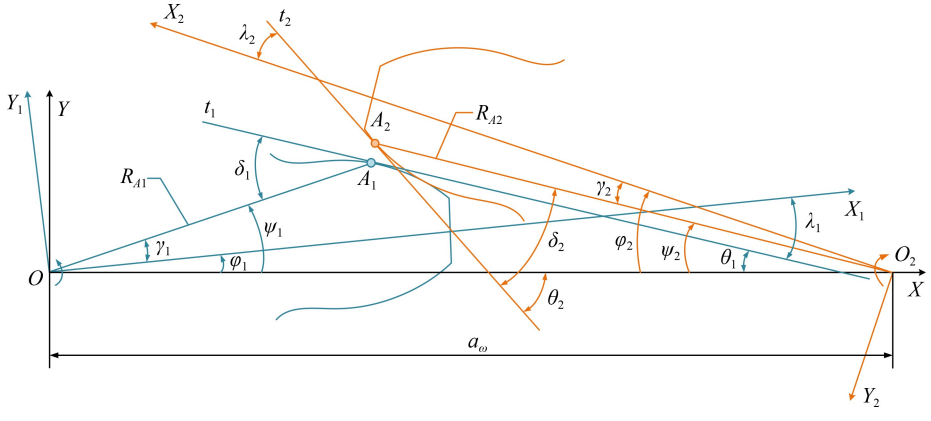


**Fig. 5** Geometric model of single-tooth meshing.

$$\theta_1 = \theta_2. \tag{11}$$

where $\theta_1$ and $\theta_2$ represent the acute angle between tangent $t_1$ and $OO_2$ and the acute angle between tangent $t_2$ and $OO_2$, respectively.

In addition to the above geometric principles and formulas, several supplementary formulas describe the geometric relationships in detail, as follows:

$$\theta_1 = \delta_1 - \psi_1, \tag{12}$$

$$\theta_2 = \delta_2 + \psi_2, \tag{13}$$

$$\psi_1 = \gamma_1 + \varphi_1, \tag{14}$$

$$\psi_2 = \varphi_2 - \gamma_2, \tag{15}$$

$$\delta_1 = \lambda_1 + \gamma_1, \tag{16}$$

$$\delta_2 = \lambda_2 + \gamma_2, \tag{17}$$

where $\delta_1$ and $\delta_2$ represent the acute angle between tangent $t_1$ and $OA_1$ and the acute angle between tangent $t_2$ and $O_2A_2$, respectively, $\psi_1$ denotes the angle between $OO_2$ and $OA_1$, where $\psi_1 > 0$ when $A_1$ is above $OO_2$ and $\psi_1 < 0$ when $A_1$ is below $OO_2$, $\psi_2$ denotes the angle between $OO_2$ and $O_2A_2$, where $\psi_2 > 0$ when $A_2$ is above $OO_2$ and $\psi_2 < 0$ when $A_2$ is below $OO_2$, $\varphi_1$ refers to the rotational angle of $X_1OY_1$ relative to $XOY$, where $\varphi_1 > 0$ when axis $X_1$ is above $OO_2$ and $\varphi_1 < 0$ when axis $X_1$ is below $OO_2$, $\varphi_2$ refers to the rotational angle of $X_2O_2Y_2$, where $\varphi_2 > 0$ when axis $X_2$ is above $OO_2$ and $\varphi_2 < 0$ when axis $X_2$ is below above $OO_2$, and $\lambda_1$ and $\lambda_2$ represent the acute angle between tangent $t_1$ and axis $X_1$ and the acute angle between tangent $t_2$ and axis $X_2$, respectively.

Gear wear changes not only the axes $Y_1$ and $Y_2$ of the meshing points $A_1$ and $A_2$ but also the slopes of the tangents $t_1$ and $t_2$. Generally, the relationship between angle $\lambda_1$ and slope $\frac{\mathrm{d}y_1}{\mathrm{d}x_1}$ can be expressed as follows:

$$\lambda_1 = \arctan\left(-\frac{\mathrm{d}y_1}{\mathrm{d}x_1}\right), \tag{18}$$

where the axis $Y_1$ of the tooth profile in the coordinate system $X_1OY_1$ can be represented by the perfect profile function $g_1(x_1)$ and the wear depth $h_{A1\_x1}$.

$$\begin{cases} y_1 = g_1(x_1) - h_{A1\_x1}, \\ \dfrac{\mathrm{d}g_1(x_1)}{\mathrm{d}x_1} = -\tan\alpha_1. \end{cases} \tag{19}$$

Therefore, substituting Eq. (19) into Eq. (18), a new geometric relationship between angle $\lambda_1$ and slope $\frac{\mathrm{d}h_{A1\_x1}}{\mathrm{d}x_1}$ can be obtained as follows:

$$\lambda_1 = \arctan\left(\tan\alpha_1 + \frac{\mathrm{d}h_{A1\_x1}}{\mathrm{d}x_1}\right). \tag{20}$$

Similarly, the new geometric relationship between angle $\lambda_2$ and slope $\frac{\mathrm{d}h_{A2\_x2}}{\mathrm{d}x_2}$ is as follows:

$$\lambda_2 = \arctan\left(\tan\alpha_1' + \frac{\mathrm{d}h_{A2\_x2}}{\mathrm{d}x_2}\right), \tag{21}$$

where $\frac{\mathrm{d}h_{A1\_x1}}{\mathrm{d}x_1}$ and $\frac{\mathrm{d}h_{A2\_x2}}{\mathrm{d}x_2}$ represent the wear slopes of the meshing points $A_1$ and $A_2$ in the local coordinate systems $X_1OY_1$ and $X_2O_2Y_2$, respectively.

According to these geometric relationships, a new mesh relationship for worn gears can be deduced. The detailed algorithm flow of the geometric model solution is as follows:

**Algorithm 1:**

1. Initialize the geometric parameters: $R_{b1}$, $R_{b2}$, $\alpha_2$, $\alpha_2'$, $a_\omega$, $h_{A1\_x1}$, $h_{A2\_x2}$, $\frac{\mathrm{d}h_{A1\_x1}}{\mathrm{d}x_1}$, $\frac{\mathrm{d}h_{A2\_x2}}{\mathrm{d}x_2}$
2. Initialize the tolerable error of the center distance and the number of meshing points: $\varepsilon_a$, NUM
3. From tooth root to tip in the driving gear: root angle $c_1$ and tip angle $a_1$
4. From tooth tip to root in the driven gear: tip angle $a_2$ and root angle $c_2$
5. **For** $i = 1, 2, \ldots,$ NUM
6. From tooth root to tip $\alpha_1 = c_1 + (a_1 - c_1)(i-1)/(\mathrm{NUM}-1)$
7. Solve directly $\alpha_1 \to \gamma_{1\mathrm{perfect}}$, $R_{A1\mathrm{perfect}}$, $\gamma_1$, $R_{A1}$, $\lambda_1$, $\delta_1$
8. **For** $j = 1, 2, \ldots,$ NUM
9. From tooth tip to root $\alpha_1' = a_2 + (c_2 - a_2)(j-1)/(\mathrm{NUM}-1)$
10. Solve directly $\alpha_1' \to \gamma_{2\mathrm{perfect}}$, $R_{A2\mathrm{perfect}}$, $\gamma_2$, $R_{A2}$, $\lambda_2$, $\delta_2$
11. Solve $\varphi_1 = \arctan\dfrac{-R_{A1}\sin\gamma_1 + R_{A2}\sin(\lambda_1 - \lambda_2 - \gamma_2)}{R_{A1}\cos\gamma_1 + R_{A2}\cos(\lambda_1 - \lambda_2 - \gamma_2)}$, $\varphi_2 = \lambda_1 - \lambda_2 - \varphi_1$
12. $\psi_1 = \gamma_1 + \varphi_1$, $\psi_2 = \varphi_2 - \gamma_2$, $\theta_1 = \delta_1 - \psi_1$, $\theta_2 = \delta_2 + \psi_2$
13. **End For**
14. Find the corresponding meshing point $\alpha_1' = \arg\min_{\alpha_1'} \left| R_{A1}\cos(\gamma_1 + \varphi_1) + R_{A2}\cos(\varphi_2 - \gamma_2) - a_\omega \right|$
15. **If** $\left| R_{A1}\cos(\gamma_1 + \varphi_1) + R_{A2}\cos(\varphi_2 - \gamma_2) - a_\omega \right| < \varepsilon_a$
16. Obtain the corresponding meshing point $\alpha_1', \gamma_{2\mathrm{perfect}}$, $R_{A2\mathrm{perfect}}$, $\gamma_2$, $R_{A2}$, $\lambda_2$, $\delta_2$
17. **Else**
18. Fail to obtain the corresponding meshing point $\alpha_1', \gamma_{2\mathrm{perfect}}$, $R_{A2\mathrm{perfect}}$, $\gamma_2$, $R_{A2}$, $\lambda_2$, $\delta_2$
19. **End If**
20. **End For**

### 2.2 Gear wear distribution

Gear wear is caused by relative sliding in gear meshing. Archard's wear model has been widely applied in the theoretical calculation of gear wear, which can be expressed as follows:

$$\frac{V}{s} = K\frac{W}{H}, \tag{22}$$

where $V$ denotes the worn volume, $s$ denotes the sliding distance, $W$ depicts the normal force, $H$ denotes the surface hardness, and $K$ is the dimensionless wear coefficient.

In our previous work [26,27], the wear distribution on the tooth profile was theoretically calculated. The results showed that gear wear depth decreases first and then increases from the tooth tip to the tooth root, as shown in Fig. 6, and increases with meshing times or running time. This paper focuses on the modeling of gear mesh relationship instead of the calculation of wear depth. Thus, the conclusion of gear wear distribution on the tooth profile is directly applied, which means that the wear depths of the gear and the pinion are directly set according to the law of wear distribution without theoretical calculation in the next section.

### 2.3 Results of mesh relationship with gear wear

In this subsection, a typical case, nonuniform wear, is illustrated to describe the geometric model with gear wear. Table 1 provides the geometric parameters and the meshing parameters of external spur gears used in the case.

Figures 7(a) and 7(b) show different nonuniform wear depths on the tooth profile of the driving and driven gears, denoted by $h_{A1\_x1}$ and $h_{A2\_x2}$, respectively. From tooth root to tip, wear depth decreases first and then increases, which is consistent with the general trend of

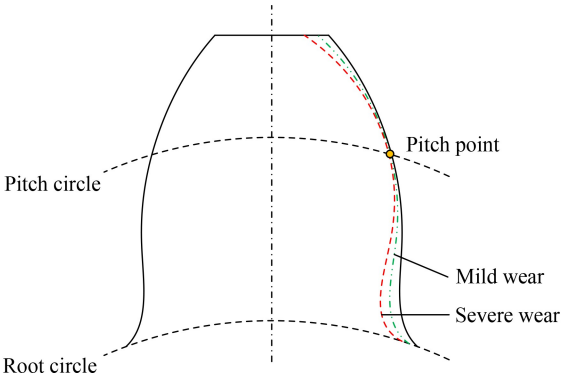


**Fig. 6** Schematic diagram of nonuniform wear.

**Table 1** Geometric parameters and meshing parameters of external spur gears

| Parameters | Driving/driven gear |
|---|---|
| Tooth number | 24/26 |
| Tooth width/mm | 50 |
| Pressure angle/(° ) | 20 |
| Module/mm | 6 |
| Poisson's ratio | 0.3 |
| Young's modulus/Pa | $2.05\times10^{11}$ |
| Base circle radius/mm | 67.7/73.3 |
| Root circle radius/mm | 64.5/70.5 |
| Center distance/mm | 150 |
| Tooth root angle, $c_1$, $c_2$/rad | 0.0714/0.0951 |
| Tooth tip angle, $a_1$, $a_2$/rad | 0.4933/0.4845 |
| Number of meshing points | 1611 |

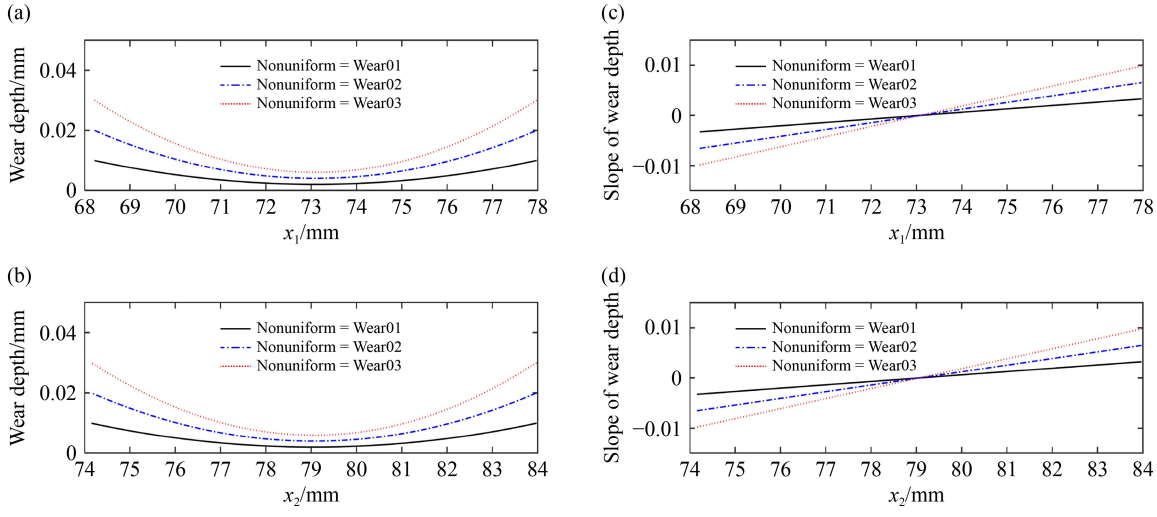


**Fig. 7** Nonuniform wear depths on tooth profile: (a) driving gear, (b) driven gear. Slopes of nonuniform wear depth on tooth profile: (c) driving gear, (d) driven gear.

gear wear evolution. Figures 7(c) and 7(d) depict different slopes of nonuniform wear depth on tooth profile of the driving and driven gears, denoted by $\frac{\mathrm{d}h_{A1\_x1}}{\mathrm{d}x_1}$ and $\frac{\mathrm{d}h_{A2\_x2}}{\mathrm{d}x_2}$. In addition, Wear01, Wear02, and Wear03 represent different degrees of nonuniform wear, namely, slight, moderate, and severe, respectively. Slight, moderate, and severe wear do not mean the definition of wear degree but only the relative relationship among the three wear states.

Based on the wear depths and its slopes, the mesh relationship can be obtained as follows: Algorithm 1. In essence, the mesh relationship consists of two parts: the position of two meshing points $A_1$ and $A_2$ on the corresponding tooth profile, denoted by $\alpha_1$ and $\alpha_1'$, and the rotational angle of two gears when two meshing points are engaged, denoted by $\varphi_1$ and $\varphi_2$. Figure 8(a) represents the single-tooth mesh relationship between $\alpha_1$ and $\alpha_1'$ with nonuniform wear, where the position of the meshing point on the tooth profile changes evidently with respect to the perfect tooth profile and $\alpha_1'$ no longer varies linearly with $\alpha_1$. The single-tooth meshing ranges of $\alpha_1$ and $\alpha_1'$ decrease with respect to the perfect tooth profile. Figure 8(b) represents the single-tooth mesh relationship between $\varphi_1$ and $\varphi_2$ with nonuniform wear, where $\varphi_2$ varies approximately linearly with $\varphi_1$, and the rotational single-tooth meshing ranges of $\varphi_1$ and $\varphi_2$ increase with respect to the perfect tooth profile.

## 3 Gear dynamic model with gear wear

In this section, the dynamic model of external spur gears with gear wear is established. Specifically, the effect of gear wear is modeled through a geometric model of a new mesh relationship. By considering the new mesh relationship, the time-varying mesh stiffness and the transmission error induced by gear wear are evaluated and further incorporated into the dynamic model to study the vibration characteristics.

### 3.1 Mechanical modeling of gear transmission

Vibration signal is generally used to monitor the state of gear wear. To understand the characteristics of vibration signal caused by gear wear, a dynamic model of external spur gears is established. The gear has the attribute of mass concentration, and the dynamic model of external spur gear pair is established by using the lumped parameter method. Figure 9 depicts a 4-DOF gear dynamic model, which contains two rotational DOFs ($\theta_1$ and $\theta_2$) and two translational DOFs ($y_1$ and $y_2$) of the gear and the pinion.

According to the dynamic model, dynamic differential equations are expressed:

$$\begin{cases} I_1\ddot{\theta}_1 + c\dot{x}_\mathrm{m}R_{\mathrm{b}1} + k(t)x_\mathrm{m}R_{\mathrm{b}1} = T_1, \\ m_1\ddot{y}_1 + c_1\dot{y}_1 + k_1y_1 - c\dot{x}_\mathrm{m} - k(t)x_\mathrm{m} = 0, \\ I_2\ddot{\theta}_2 - c\dot{x}_\mathrm{m}R_{\mathrm{b}2} - k(t)x_\mathrm{m}R_{\mathrm{b}2} = -T_2, \\ m_2\ddot{y}_2 + c_2\dot{y}_2 + k_2y_2 + c\dot{x}_\mathrm{m} + k(t)x_\mathrm{m} = 0, \end{cases} \tag{23}$$

where $x_\mathrm{m}$ is the relative displacement of two gears, $I_1$ and $I_2$ are the moments of inertia of the gear and the pinion, respectively, $m_1$ and $m_2$ are the masses of the gear and the pinion, respectively, $k_1$ and $k_2$ are the supporting stiffnesses of the gear and the pinion, respectively, $k(t)$ and $c$ are the time-varying mesh stiffness and mesh damping, respectively, and $T_1$ and $T_2$ are the input torque of the gear and the load torque of the pinion, respectively.

The relative displacement of two gears is as follows:

$$x_\mathrm{m} = R_{\mathrm{b}1}\theta_1 - R_{\mathrm{b}2}\theta_2 - y_1 + y_2 - e(t). \tag{24}$$

In gear dynamics, $e(t)$ is the unloaded static transmission error (USTE), and it mainly includes manufacturing error, tooth profile error, and gear failure. Thus, USTE can be divided into long period error $e_{A1}(t)$, short period error $e_{A2}(t)$, random error $e_{\mathrm{error}}(t)$, and gear failure error $e_{\mathrm{wear}}(t)$ caused by gear wear.

$$e(t) = e_{A1}(t) + e_{A2}(t) + e_{\mathrm{error}}(t) + e_{\mathrm{wear}}(t), \tag{25}$$

$$\begin{cases} e_{A1}(t) = A_1\sin(2\pi f_1 t), \\ e_{A2}(t) = A_2\sin(2\pi f_\mathrm{m} t), \\ e_{\mathrm{error}}(t) = 0.2\mathrm{rand}, \end{cases} \tag{26}$$

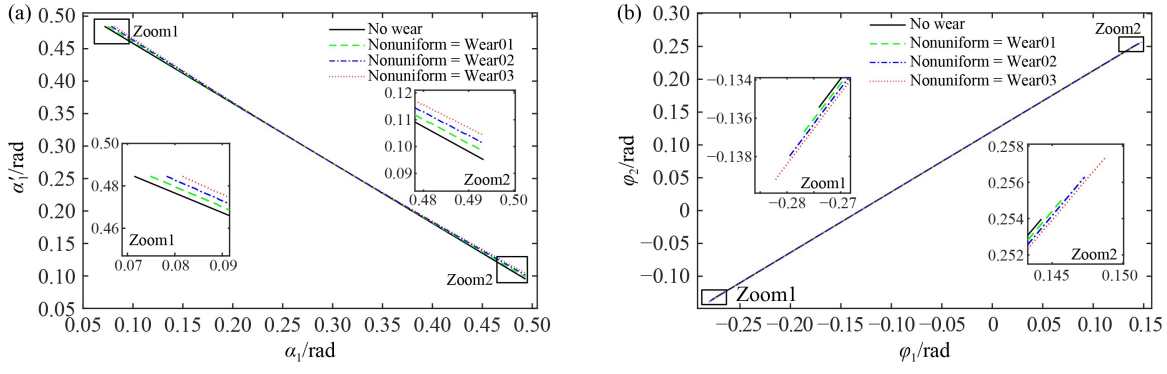


**Fig. 8** Single-tooth mesh relationship with nonuniform wear: (a) mesh relationship between $\alpha_1$ and $\alpha_1'$, (b) mesh relationship between $\varphi_1$ and $\varphi_2$.

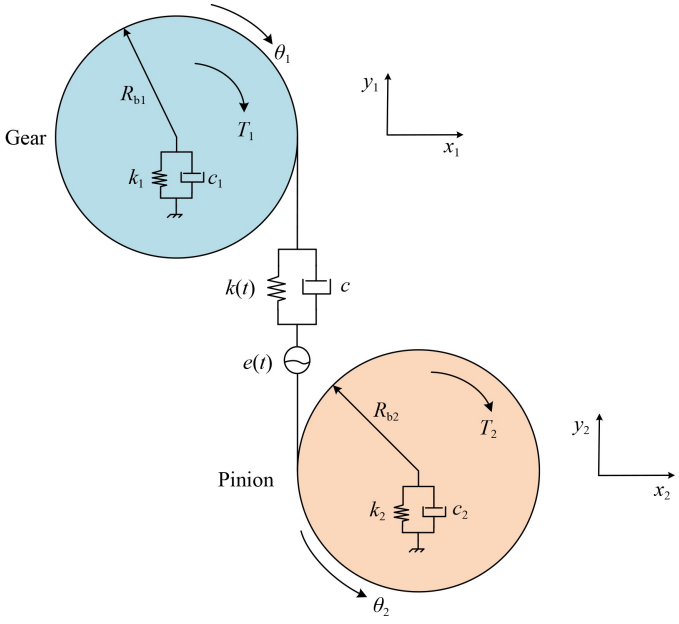


**Fig. 9** Dynamic model of external spur gear pair.

where $f_1$ and $f_m$ are the rotational frequency and the meshing frequency, respectively, $A_1$ and $A_2$ are the amplitude of long period and short period, respectively, $A_1$ and $A_2$ are set to 30 and 15 μm, respectively, and "rand" is the random number in the range [0, 1]. The dynamic parameters of external spur gears are listed as follows:

Input torque: 1300 N·m;

Output torque: 1267.5 N·m;

Supporting stiffness: $6.56\times10^7$ N/m;

Supporting damping: $1.8\times10^5$ N·m$^{-1}$·s.

The gear wear in the dynamic model is coupled through the meshing excitations including mesh stiffness and transmission error, whose evaluation is presented in the following subsections.

### 3.2 Mesh stiffness considering new mesh relationship

Generally, the variation of gear mesh stiffness is used as an important basis for gear dynamic analysis. In this section, the mesh stiffness of external spur gears with gear wear is evaluated through the deduced new mesh relationship. First, based on the new mesh relationship and the potential energy method, the single-tooth mesh stiffness with gear wear is evaluated in the typical case of nonuniform wear. Then, according to the multiteeth mesh rule, the multiteeth mesh stiffness is evaluated through the superposition of the single-tooth meshing stiffness.

#### 3.2.1 Single-tooth mesh stiffness

Mesh stiffness excitation is the crucial internal excitation of gear meshing and usually regarded as the main influence factor of gear failures on gear dynamics, such as tooth crack and spalling [28–30]. Thus, the influence of gear wear on mesh stiffness is analyzed through the new mesh relationship obtained in Section 2.3. The potential energy method is adopted in the calculation of mesh stiffness, where the tooth is considered a cantilever beam. In Ref. [26], the stiffness included Hertzian contact stiffness $k_h$, bending stiffness $k_b$, shear deformation stiffness $k_s$, and axial compressive stiffness $k_a$. Furthermore, the stiffness with gear wear is deduced and calculated.

External spur gear contains two situations in the calculation of mesh stiffness, Situation 1: $R_{b1} > R_{r1}$ and Situation 2: $R_{b1} \leqslant R_{r1}$, as shown in Figs. 10(a) and 10(b), respectively, where $R_{r1}$ is the radius of the root circle. These figures show that gear wear changes not only the height of the tooth profile at positions $d$ and $x$ denoted by $h$ and $h_x$, respectively, but also the direction of force $F$, denoted by $\lambda_1$.

When a pair of teeth is engaged, the single-tooth mesh stiffness can be deduced through the superposition of the single-tooth stiffness of two teeth and expressed as follows:

$$k = \frac{1}{\frac{1}{k_h}+\frac{1}{k_{b1}}+\frac{1}{k_{s1}}+\frac{1}{k_{a1}}+\frac{1}{k_{f1}}+\frac{1}{k_{b2}}+\frac{1}{k_{s2}}+\frac{1}{k_{a2}}+\frac{1}{k_{f2}}}, \quad (27)$$

where subscripts 1 and 2 represent the single-tooth stiffness of two meshing points $A_1$ and $A_2$ in the driving and driven gears, respectively.

Gear parameters and wear depths are the same as the case studies in Section 2.3. According to the new mesh relationship, as shown in Fig. 8, and the single-tooth stiffness, the single-tooth mesh stiffness can be gained. Figure 11 shows the single-tooth mesh stiffness of $\varphi_1$ with different nonuniform wear depths, where $\varphi_1$ represents the

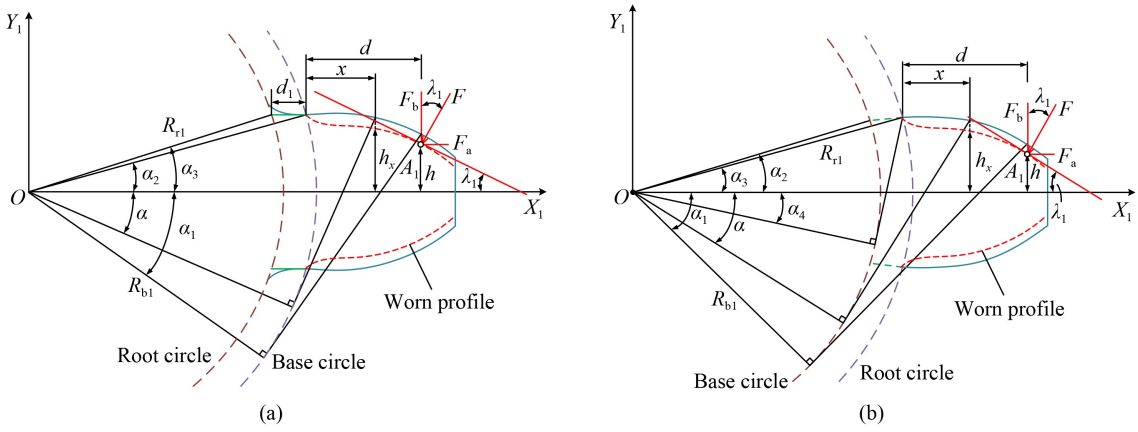


**Fig. 10** Beam model of a single tooth with worn profile. (a) $R_{b1} > R_{r1}$; (b) $R_{b1} \leqslant R_{r1}$.

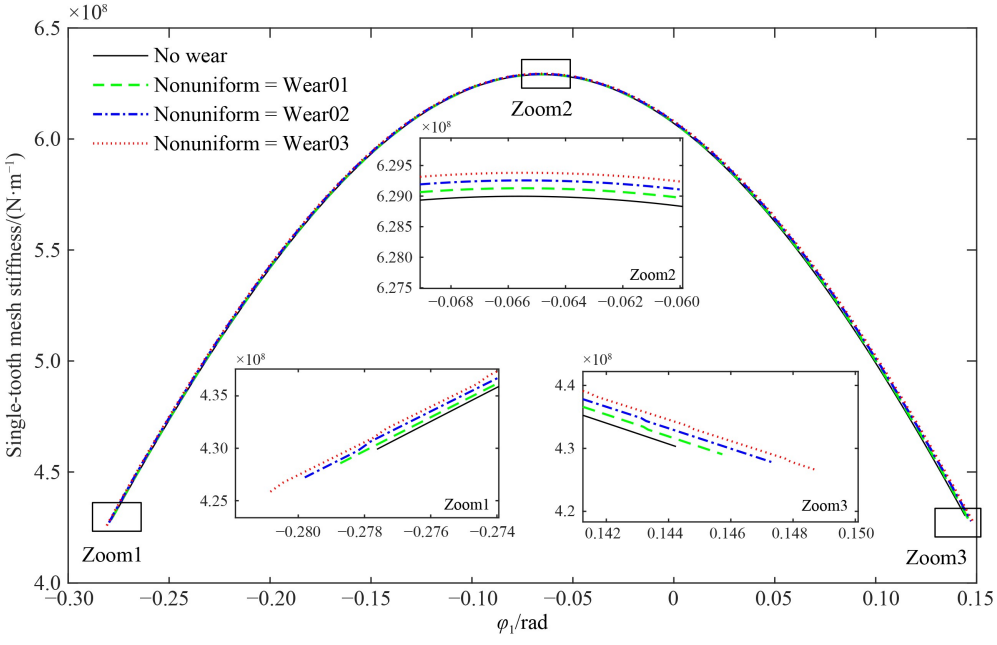


**Fig. 11** Single-tooth mesh stiffness of $\varphi_1$ with different nonuniform wear depths.

rotational angle of the driving gear and is obtained through the new mesh relationship, as shown in Fig. 8. The single-tooth mesh stiffness of $\varphi_1$ increases with increasing wear depth slightly while the rotational meshing range increases with increasing wear depth.

### 3.2.2 Multiteeth mesh stiffness

For gear transmission of external spur gears, the single tooth and the double teeth of gears are alternately engaged. To obtain the rule of gear meshing with gear wear, the relationship between single tooth and double teeth, which is called the multiteeth mesh rule in this paper, is introduced and deduced.

According to the new single-tooth mesh relationship in Section 2.3, the mesh relationship between rotational angles of the driving and driven gears, denoted by $\varphi_1$ and $\varphi_2$, respectively, can be gained. Figure 12 shows the mesh relationship of single tooth and multiple teeth with the perfect tooth profile, where the multiteeth meshing range is obtained by superposition of the single-tooth meshing range and derived as follows:

$$\begin{cases} \varphi_1\left(2^{\text{nd}}\right) = \varphi_1\left(1^{\text{st}}\right) + \dfrac{2\pi}{z_1}, \\ \varphi_2\left(2^{\text{nd}}\right) = \varphi_2\left(1^{\text{st}}\right) + \dfrac{2\pi}{z_2}, \end{cases} \begin{cases} \varphi_1\left(3^{\text{rd}}\right) = \varphi_1\left(1^{\text{st}}\right) + 2\times\dfrac{2\pi}{z_1}, \\ \varphi_2\left(3^{\text{rd}}\right) = \varphi_2\left(1^{\text{st}}\right) + 2\times\dfrac{2\pi}{z_2}, \end{cases} \cdots \begin{cases} \varphi_1\left(n^{\text{th}}\right) = \varphi_1\left(1^{\text{st}}\right) + (n-1)\dfrac{2\pi}{z_1}, \\ \varphi_2\left(n^{\text{th}}\right) = \varphi_2\left(1^{\text{st}}\right) + (n-1)\dfrac{2\pi}{z_2}, \end{cases} \tag{28}$$

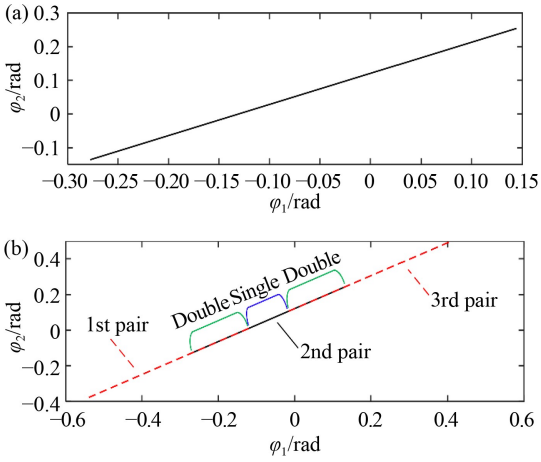


**Fig. 12** Tooth mesh relationship with perfect tooth profile: (a) single-tooth, (b) multiteeth.

where $z_1$ and $z_2$ are the tooth numbers of the driving and driven gears, respectively, and $n^{\text{th}}$ represents the $n$th tooth pair.

In Fig. 12(b), single-tooth meshing, taking the second pair as an example, can be divided into three parts in multiteeth meshing, double–single–double, where double indicates that two pairs of teeth mesh simultaneously, and single means that a pair of teeth meshes. To obtain the multiteeth mesh relationship with gear wear, the multiteeth mesh rule contains two principles:

(1) With the increase of $\varphi_1$, the tooth pair with larger $\varphi_2$ meshes first in the double-teeth meshing range.

(2) When $\Delta\varphi_2 < Threshold$ for the same $\varphi_1$, two pairs of teeth mesh simultaneously. *Threshold* is the threshold of the tolerable error of rotational angle and it is set to $10^{-4}$ rad in this paper.

According to the single-tooth mesh relationship in Fig. 8 and the multiteeth mesh rule, the multiteeth mesh relationship with nonuniform wear can be obtained, taking Wear01 as the example, as shown in Fig. 13. With the multiteeth mesh rule, the mesh relationship of the first, second, and third tooth pairs between $\varphi_1$ and $\varphi_2$ can be obtained, as shown in Fig. 13(a). Next, the double-teeth meshing range of the first and second tooth pairs is enlarged, as shown in Fig. 13(b), where $\Delta\varphi_2$ exists between two pairs. Through two principles of the multiteeth mesh rule, *Threshold* is set to $10^{-4}$ rad, and the new double-teeth meshing range is obtained, as shown in Fig. 13(c). Thus, the double–single–double meshing range is revised in Fig. 13(d), and the meshing range of the second tooth pair is reduced, where the single-tooth meshing range increases and the double-teeth meshing range decreases.

The results indicate that the multiteeth mesh relationship affects the single-tooth meshing range in Section 2.3.1. Therefore, the new single-tooth mesh stiffness with the new single-tooth meshing range can be obtained, as

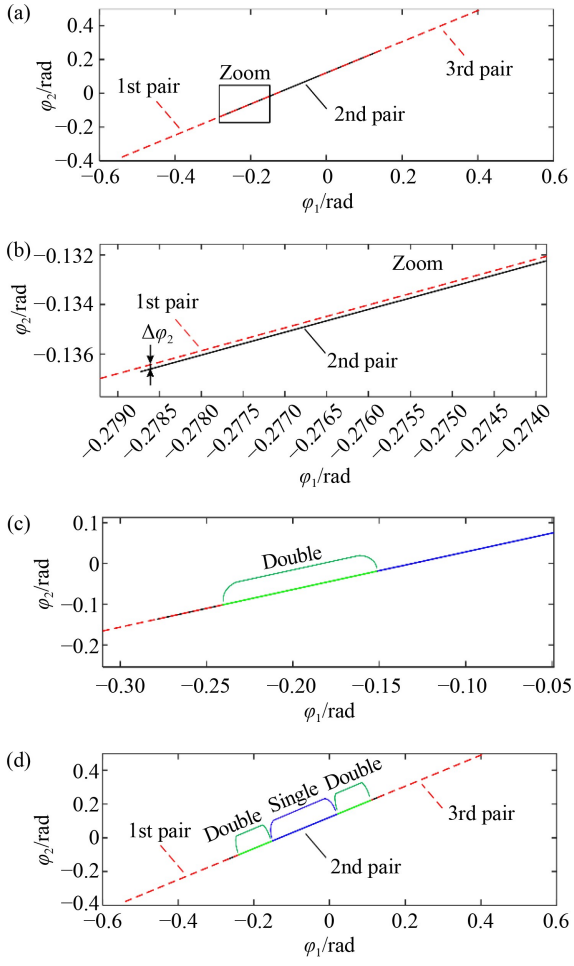


**Fig. 13** Multiteeth mesh relationship with nonuniform wear (Wear01): (a) multiteeth, (b) zoom of (a), (c) double-teeth meshing range of (b), and (d) double–single–double meshing range.

shown in Fig. 14. Compared with the original mesh stiffness, the new mesh stiffness only changes the meshing range of a tooth pair, denoted by $\varphi_1$.

According to the new single-tooth mesh stiffness and the multiteeth mesh relationship deduced through the multiteeth mesh rule, the multiteeth mesh stiffness and the expression of double-teeth mesh stiffness can be derived and calculated as follows:

$$k = \sum_{i=1}^{2} \frac{1}{\frac{1}{k_{\mathrm{h},i}} + \frac{1}{k_{\mathrm{b1},i}} + \frac{1}{k_{\mathrm{s1},i}} + \frac{1}{k_{\mathrm{a1},i}} + \frac{1}{k_{\mathrm{f1},i}} + \frac{1}{k_{\mathrm{b2},i}} + \frac{1}{k_{\mathrm{s2},i}} + \frac{1}{k_{\mathrm{a2},i}} + \frac{1}{k_{\mathrm{f2},i}}}, \tag{29}$$

where subscript $i$ ($i$ = 1, 2) depicts the number of the meshing tooth pair.

Figure 15 shows the multiteeth meshing stiffness, where nonuniform tooth wear mainly changes single-tooth and double-teeth meshing ranges, and its influence on the amplitude is negligible.

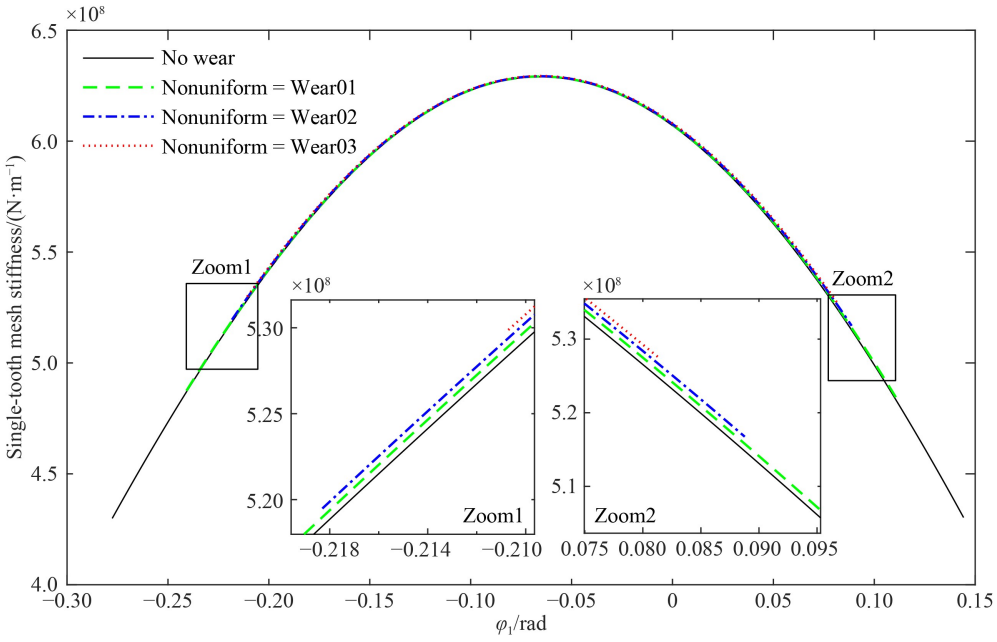


**Fig. 14** Single-tooth mesh stiffness with the new single-tooth mesh relationship.

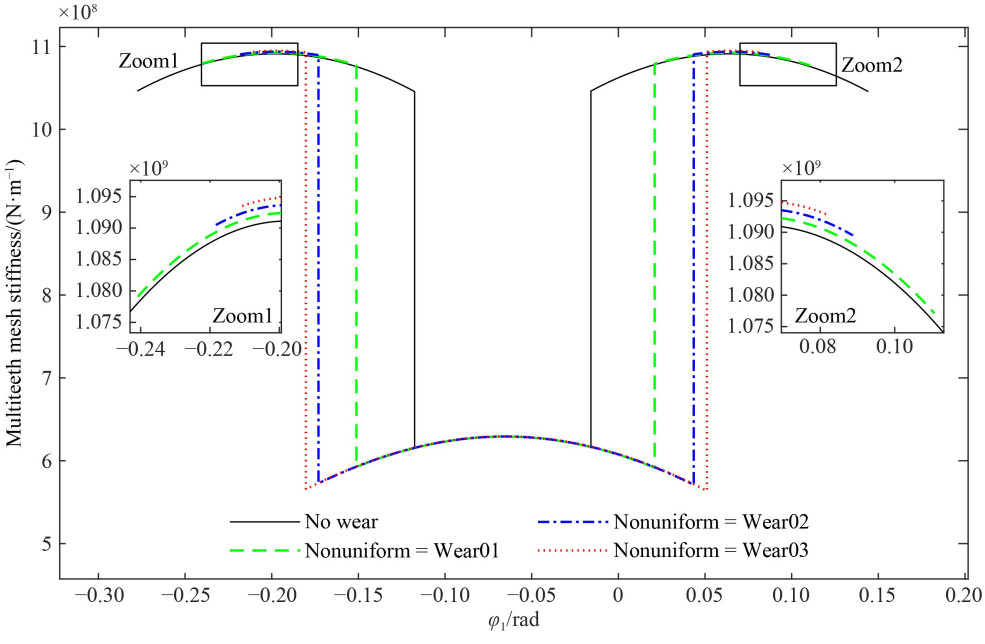


**Fig. 15** Multiteeth mesh stiffness with nonuniform wear.

### 3.2.3 Verification of mesh stiffness

To verify the results of multiteeth mesh stiffness with nonuniform wear, ANSYS is used for finite element analysis and model verification; this verification strategy has been widely used to verify the mesh stiffness of gears with crack and spalling faults [31,32]. Furthermore, the flow of finite element method is introduced.

(1) Establish the 3D model of gears

To reduce the amount of calculation, the gear model is established. To verify different wear depths, two gear models are established: perfect profile and nonuniform wear (Wear01). First, the 2D gear plane is constructed according to the discrete points of the normal and worn tooth profile curves. Then, the 2D gear plane is extruded into a 3D gear model.

(2) Mesh the gears

To reduce the amount of calculation, Solid185 element is adopted to mesh different parts of gears with different mesh densities, where the multiteeth mesh is the densest.

(3) Define rigid regions

To force the gears to rotate around the shaft, all nodes of each gear bore are fixed on corresponding shaft centers, $O$ and $O_2$, which are defined by the mass element Mass21.

(4) Create tooth contact pairs

To avoid tooth interference during gear meshing, tooth contact pairs are created for the tooth surface of the driving and driven gears, where the contact elements are Conta174 and Targe170.

(5) Apply loads and define boundary conditions

Except for the rotational DOF around the $Z$ axis, the remaining DOFs of $O$ (Mass21) are fixed. Moreover, all DOFs of $O_2$ (Mass21) are fixed. $Z$-axis moment $T$ is applied at node $O$.

Finally, the finite element model of two gears is established, as shown in Fig. 16, and the angular displacement $\theta$ at node $O$ is solved. Thus, mesh stiffness can be derived as follows:

$$K = \frac{T}{R_{b1}^2 \theta}. \tag{30}$$

The result of multiteeth mesh stiffness with nonuniform wear is shown in Fig. 17, which depicts the mesh stiffness of theoretical calculation and the finite element verification with nonuniform wear (Wear01), where the double–single–double meshing ranges of the two are the same and the mesh stiffness of the two in the single-tooth meshing range are the same while the mesh stiffness of the two in the double-tooth meshing range are different in its amplitude.

Therefore, through the finite element model, the multiteeth mesh stiffness is verified, and the geometric model of external spur gears with wear in the typical case of nonuniform wear is indirectly verified.

### 3.3 Unloaded static transmission error considering new mesh relationship

In the above theoretical derivation for the geometric

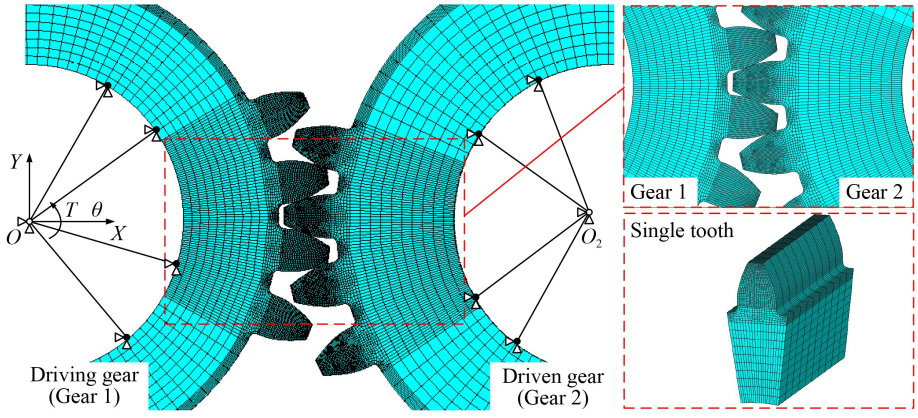


**Fig. 16** Finite element model of gear pair.

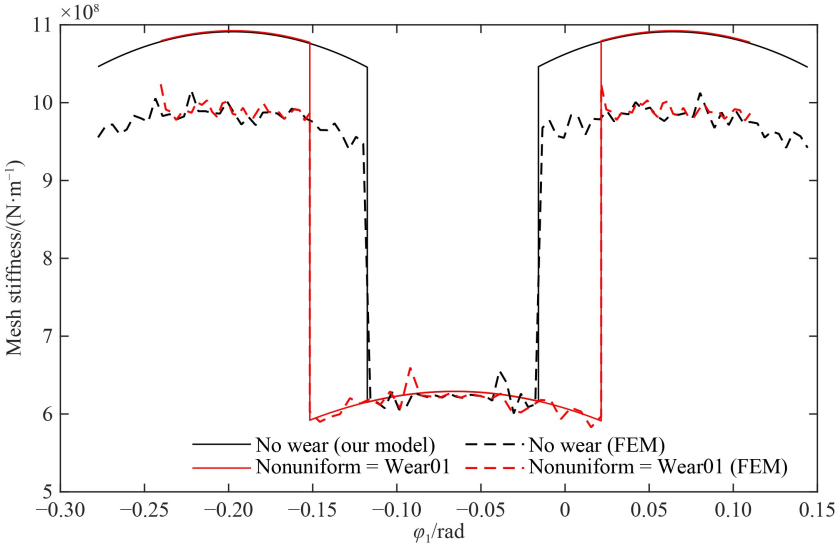


**Fig. 17** Mesh stiffness of theoretical calculation and finite element verification (no wear and Wear01).

model of external spur gears with gear wear, the new mesh relationship is gained. Therefore, the new mesh relationship is utilized to deduce the USTE.

As described in dynamic model of Subsection 3.1, USTE represents the deviation between the actual position and the theoretical position of the driven gear under unloaded condition, which is usually caused by tooth profile error and assembly error. The USTE caused by gear wear is expressed as follows:

$$e_{\text{wear}} = \frac{R_{\text{b1}}}{R_{\text{b2}}}\varphi_1 - \varphi_2. \tag{31}$$

USTE changes because gear wear alters the mesh relationship. Based on the new mesh relationship between $\varphi_1$ and $\varphi_2$, the USTE with gear wear can be directly derived. The results are shown in Fig. 18, where USTE varies periodically with meshing frequency, and amplitude increases with increasing wear depth.

## 4 Vibration characteristics of gear transmission with gear wear

Based on the established dynamic model, including mesh stiffness and USTE, the vibration characteristics of gear wear are obtained. To reflect the dynamic responses of different wear states, 50 sets of wear states are simulated. In the 50 sets of wear states, the maximum wear depth of each state in two gears is set to 0.005NUM mm, and NUM (NUM = 0, 1, 2, ..., 49) is the number of the set, which means that the maximum wear depth ranges from 0 to 0.25 mm. With wear depths in different wear states, mesh stiffness and USTE with gear wear are incorporated into the dynamic model, and these equations are solved to obtain dynamic responses. The geometric parameters are listed in Table 1, the rotational frequency of the driving gear $f_{\text{i}}$ = 16.64 Hz, and meshing frequency $f_{\text{m}}$ = 399.4 Hz. The dynamic response characteristics of gear wear are described from four aspects: time-domain, frequency-domain, envelope frequency-domain, and condition indicators. Figures 19(a) and 19(b) are time-domain signals when NUM = 0 and NUM = 40, where the amplitude of vibration impact is clearly increased with increasing wear depth. Moreover, the interval time between two impacts in a meshing period is changed due to the variation of the meshing range of mesh stiffness, which is caused by the new mesh relationship of gear wear. In the frequency-domain signals of different wear depths, as shown in Figs. 20(a) and 20(b), the meshing frequencies and their sidebands of rotational frequency are the main components, and gear wear only changes the frequency amplitudes but not the frequency structure in the spectrum. Similarly, in envelope frequency-domain signals of different wear depth, as shown in Fig. 21(a) and 21(b), the amplitudes of the meshing frequencies and their sidebands of rotational frequency are increased with increasing wear depth. Generally, evident fault characteristic frequency is observed in the vibration signal for gear wear. Thus, condition indicator (CI) is generally utilized to monitor the wear state. Root-mean-square (RMS), kurtosis (Kur), and first-order meshing frequency amplitude (OMX) are used to monitor the wear state under different wear depths. Figure 22 shows the variations of CIs with different wear depths, where RMS represents the average vibration level and gear wear leads to the increase of RMS, Kur depicts the vibration impact

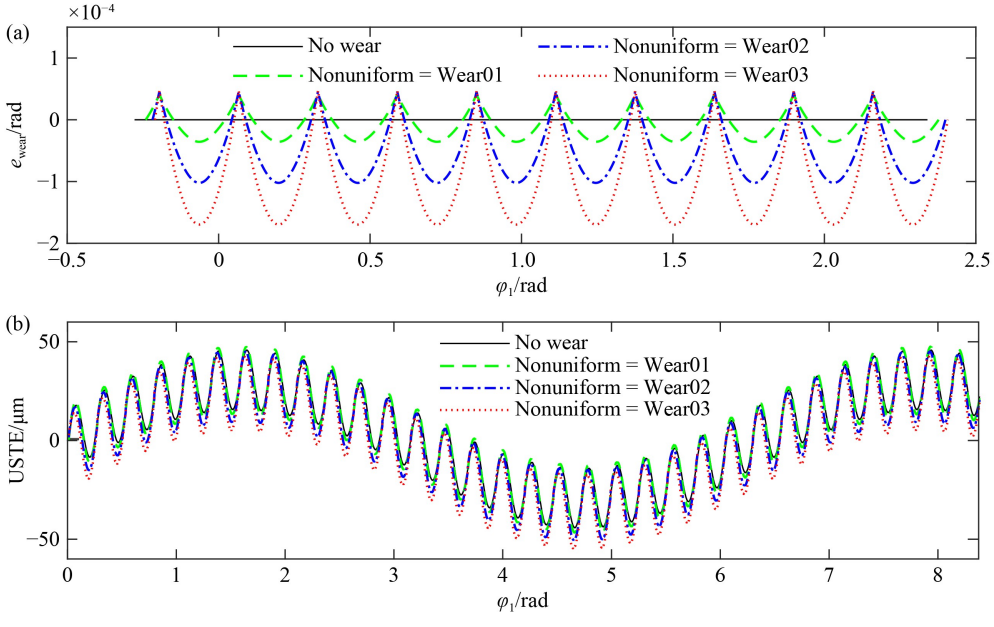


**Fig. 18** USTE of nonuniform wear with different wear depths: (a) $e_{\text{wear}}$, (b) USTE.

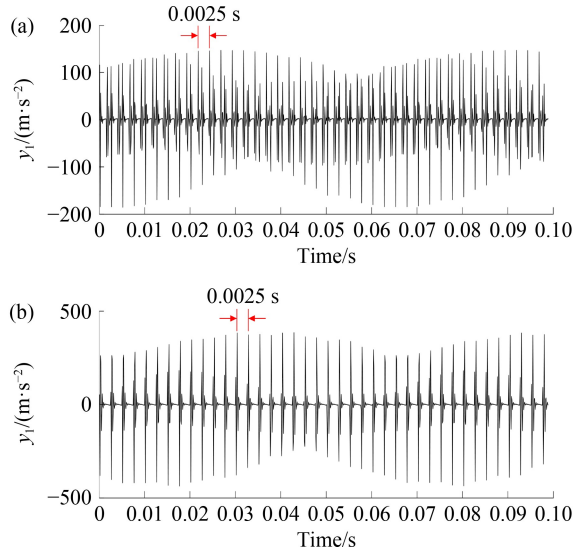


**Fig. 19** Simulated time-domain signal with different wear depths: (a) NUM = 0, (b) NUM = 40.

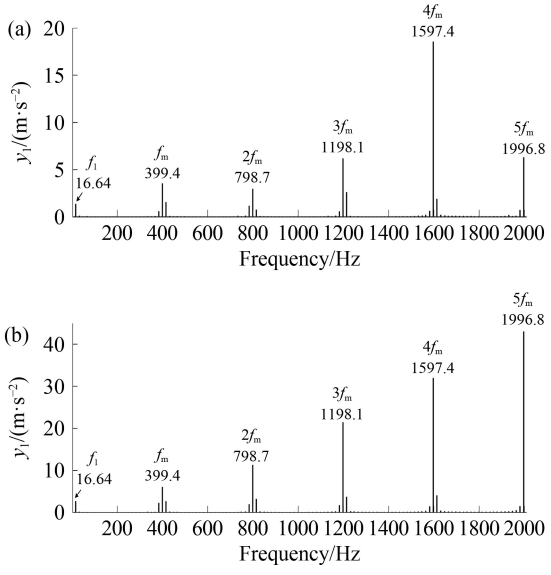


**Fig. 20** Simulated frequency-domain signal with different wear depths: (a) NUM = 0, (b) NUM = 40.

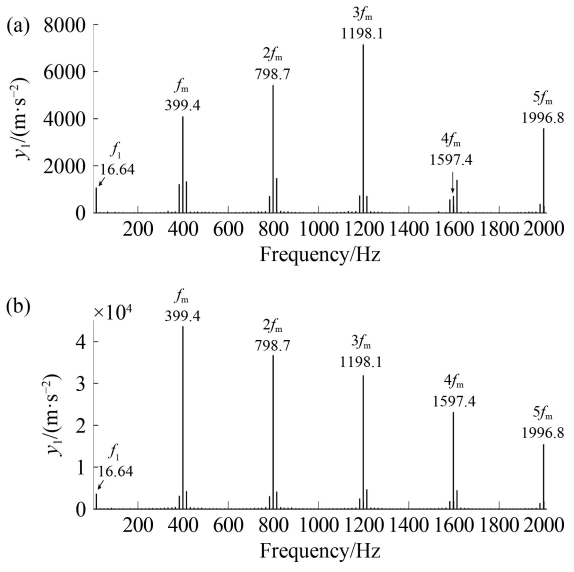


**Fig. 21** Simulated envelope frequency-domain signal with different wear depths: (a) NUM = 0, (b) NUM = 40.

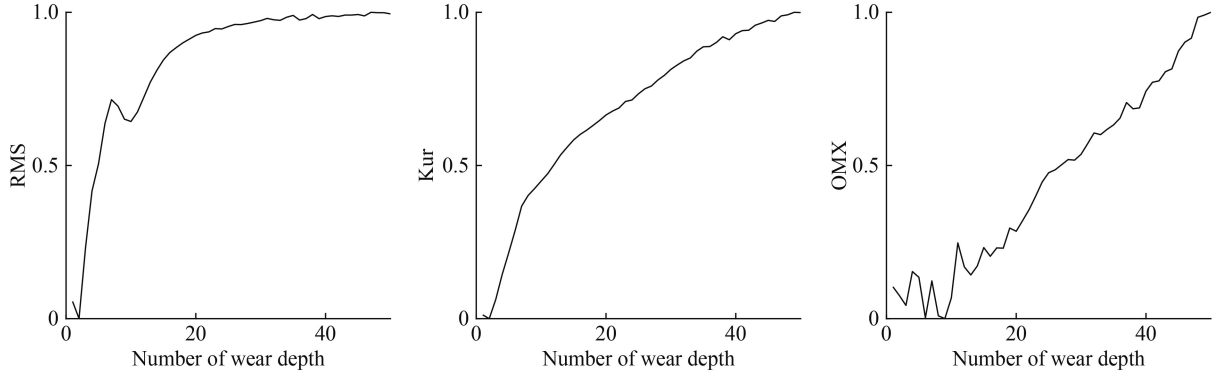


**Fig. 22** Condition indicators with different wear depths.

level and gear wear results in the increase of Kur, and OMX increases with gear wear.

$$\mathrm{RMS} = \sqrt{\frac{1}{N}\sum_{n=1}^{N} x^2(n)},\ \mathrm{Kur} = E\left[\left(\frac{x-\mu}{\sigma}\right)^4\right], \tag{32}$$

where $x$ is the signal, $\mu$ and $\sigma$ indicate the mean and the standard deviation of the signal, respectively.

## 5 Experimental studies

In the experimental test, an open-source dataset about gear fatigue life [33] is adopted to simulate the variation of gear wear. Figure 23 shows the structure of gear transmission. It contains two gear pairs, and the numbers of teeth are $Z_1 = Z_4 = 24$ and $Z_2 = Z_3 = 26$ while rotational frequency and meshing frequency are the same as the simulations in the dynamic model. The dataset includes 600 segments of data (Data_NUM = 1, 2, ..., 600), each

segment is 10 s per minute, and gear pitting failure finally occurs. In gear fatigue life, gear wear is difficult to avoid, and inducing serious faults, such as pitting, is easy. Thus, dataset (20190507_1200_1000_geardegp4_10-60) is used to verify vibration characteristics of gear wear.

Figures 24(a) and 24(b) are the time-domain signals when Data_NUM = 1 and Data_NUM = 400, respectively, where no substantial change in the signal is observed. In frequency-domain and envelope frequency-domain signal, as shown in Figs. 25 and 26, the meshing frequencies and their harmonics are the main components in the spectrum. With the increase of running time, the structure of the spectrum lacks considerable change because gear wear has no fault characteristic frequency. However, the amplitude of the meshing frequencies and their sidebands changes clearly. CIs are an effective method to monitor gear wear state by vibration signal. Figure 27 shows the variations of CIs with the increase of running time, and their trends are consistent with the simulation results.

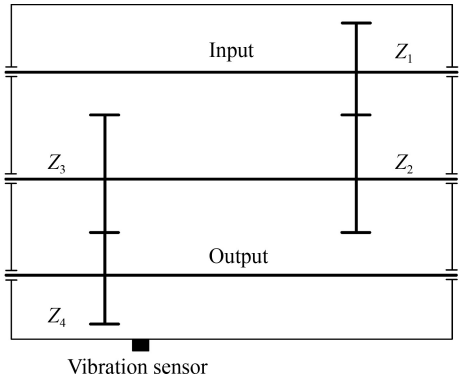


**Fig. 23** Schematic diagram of experimental transmission.

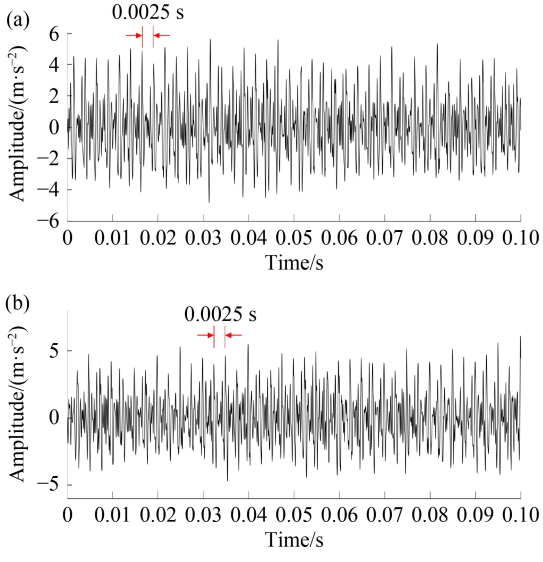


**Fig. 24** Experimental time-domain signal with different wear depths: (a) Data_NUM = 1, (b) Data_NUM = 400.

Gear wear does not change the structure of the spectrum due to the lack of fault characteristic frequency, but the amplitude of the meshing frequency and its sidebands change apparently, which can be regarded as the basis for building a new CI. In addition, RMS, Kur, and OMX increase with increasing running time, which is an important basis for judging the gear running state.

## 6 Conclusions

In this paper, a geometric model of gear meshing is proposed to depict the new mesh relationship caused by

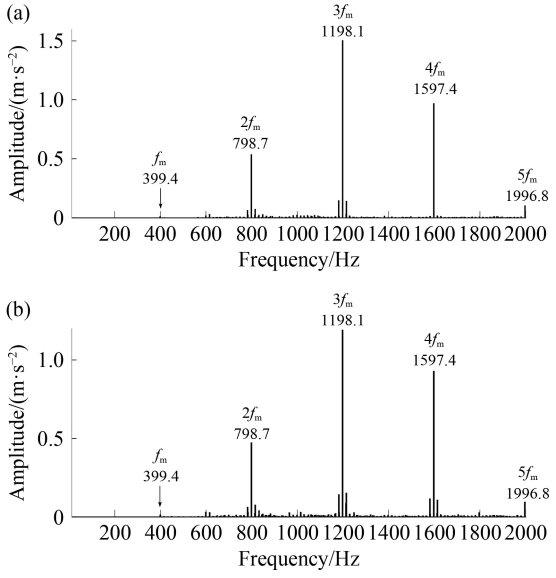


**Fig. 25** Experimental frequency-domain signal with different wear depths: (a) Data_NUM = 1, (b) Data_NUM = 400.

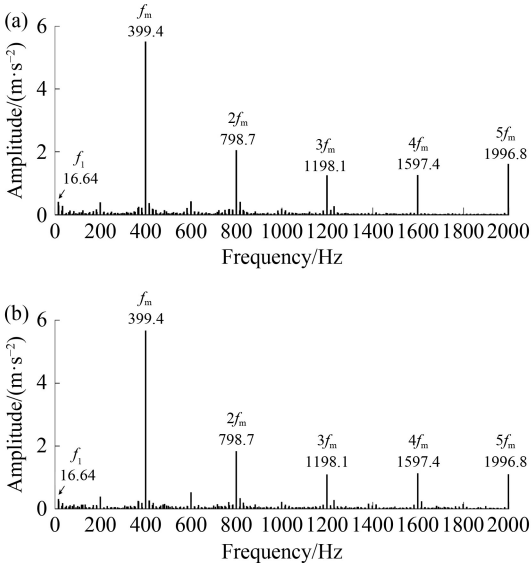


**Fig. 26** Experimental envelope frequency-domain signal with different wear depths: (a) Data_NUM = 1, (b) Data_NUM = 400.

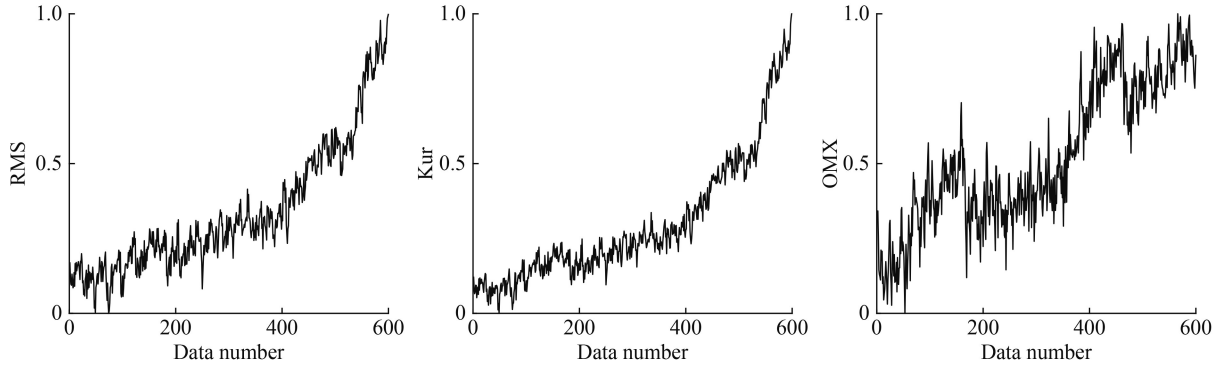


**Fig. 27** Condition indicators with different segments.

gear wear. Subsequently, the dynamic model for external spur gears with gear wear is established based on the proposed geometric model. Considering the new mesh relationship, the effects of gear wear on mesh stiffness and transmission error are comprehensively analyzed. The results indicate that in the typical case of nonuniform wear, gear wear mainly changes the single-tooth and double-teeth meshing ranges of mesh stiffness, and its influence on the amplitude of mesh stiffness is negligible. Furthermore, the vibration characteristics of gear wear are revealed with numerical and experimental studies. The results suggest that gear wear changes the interval time between two impacts in a meshing period, which is caused by the variation of the gear mesh relationship. Gear wear does not change the structure of the spectrum, but it alters the amplitude of the meshing frequencies and their sidebands. In addition, the effects of gear wear on several vibration features, such as RMS, Kur, and OMX, are comparatively investigated. The results indicate that these features present a consistent increasing tendency with the increase of wear depth and running time, that is, they can serve as condition indicators for gear wear monitoring.

Furthermore, for conditions coupling gear wear with other gear faults, the new mesh relationship obtained through the proposed model may offer several bases for the dynamic modeling and analysis of gear transmission systems with multiple faults. These topics will be discussed in our future works.

## Nomenclature

| | |
|---|---|
| $a_1$, $a_2$ | Tip angles of gear and pinion, respectively |
| $a_\omega$ | Center distance of two gears |
| $A_1$, $A_2$ | Amplitude of long period and short period, respectively |
| $A_{1\text{perfect}}$, $A_1$ | Meshing points on the perfect profile and the worn profile of the driving gear, respectively |
| $A_{2\text{perfect}}$, $A_2$ | Meshing points on the perfect profile and the worn profile of the driven gear, respectively |
| $c$ | Time-varying mesh damping |
| $c_1$, $c_2$ | Root angles of gear and pinion or supporting damping of gear and pinion |
| $e(t)$ | Unloaded static transmission error |
| $e_{A1}(t)$, $e_{A2}(t)$ | Long and short period errors, respectively |
| $e_{\text{error}}(t)$ | Random error |
| $e_{\text{wear}}(t)$ | Gear failure error caused by gear wear |
| $f_1$, $f_\text{m}$ | Rotational frequency and meshing frequency, respectively |
| $F$ | Force |
| $g_1(x_1)$ | Perfect profile function |
| $h$, $h_x$ | Heights of the tooth profile at positions $d$ and $x$, respectively |
| $h_{A1\_x1}$, $h_{A2\_x2}$ | Wear depth in the perfect meshing point $A_{1\text{perfect}}$ and $A_{2\text{perfect}}$, respectively |
| $H$ | Surface hardness |
| $I_1$, $I_2$ | Moments of inertia of gear and pinion, respectively |
| $k$ | Mesh stiffness |
| $k_1$, $k_2$ | Supporting stiffnesses of gear and pinion, respectively |
| $k_\text{a}$, $k_\text{b}$, $k_\text{h}$, $k_\text{s}$ | Axial compressive stiffness, bending stiffness, Hertzian contact stiffness, shear deformation stiffness, respectively |
| $k(t)$ | Time-varying mesh stiffness |
| $K$ | Dimensionless wear coefficient or mesh stiffness |
| $m_1$, $m_2$ | Masses of two gears |
| $n^{\text{th}}$ | The $n$th tooth pair |
| $N_1N_2$ | Ideal meshing line |
| NUM, Data_NUM | Number of discrete meshing points and number of experimental set, respectively |
| $O_1$, $O_2$ | Geometric center of two gears |
| rand | Random number in the range [1, 0] |
| $R_1$, $R_2$ | Radii of the pitch circle |
| $R_{A1\text{perfect}}$, $R_{A1}$ | Radii of the meshing points $A_{1\text{perfect}}$ and $A_1$, respectively |
| $R_{A2\text{perfect}}$, $R_{A2}$ | Radii of the meshing points $A_{2\text{perfect}}$ and $A_2$, respectively |
| $R_\text{b1}$, $R_\text{b2}$ | Radii of the base circle |

| | |
|---|---|
| $R_{f1}$ | Radius of the root circle |
| $s$ | Sliding distance |
| $t_1$, $t_2$ | Tangents of two meshing points |
| $T$ | Moment |
| $T_1$ | Input torque of the gear |
| $T_2$ | Load torque of the pinion |
| *Threshold* | Threshold of the tolerable error of rotational angle |
| $V$ | Worn volume |
| $W$ | Normal force |
| $x$ | Signal |
| $x_1$, $x_2$ | Abscissa values of the coordinate systems $X_1OY_1$ and $X_2O_2Y_2$ or translational DOFs of gear and pinion, respectively |
| $x_m$ | Relative displacement of two gears |
| $XOY$ | Fixed global coordinate system |
| $X_1OY_1$, $X_2O_2Y_2$ | Local coordinate systems rotating with the driving and driven gears, respectively |
| $y_1$, $y_2$ | Ordinate values of the coordinate systems $X_1OY_1$ and $X_2O_2Y_2$ or translational DOFs of gear and pinion, respectively |
| $z_1$, $z_2$ | Tooth number of two gears |
| $Z_1$, $Z_2$, $Z_3$, $Z_4$ | Tooth number in experiments |
| $\alpha_2$, $\alpha_1$ | Angles of the base circle and the perfect meshing point $A_{1perfect}$ on the single-tooth profile, respectively |
| $\alpha_2'$, $\alpha_1'$ | Angles of the base circle and the perfect meshing point $A_{2perfect}$ on the single-tooth profile, respectively |
| $\gamma_{1perfect}$, $\gamma_1$ | Angles of the perfect meshing point $A_{1perfect}$ and the worn meshing point $A_1$, respectively |
| $\gamma_{2perfect}$, $\gamma_2$ | Angles of the perfect meshing point $A_{2perfect}$ and the worn meshing point $A_2$, respectively |
| $\theta$ | Angular displacement |
| $\theta_1$, $\theta_2$ | Acute angle between tangent $t_1$ and $OO_2$ and the acute angle between tangent $t_2$ and $OO_2$, or rotational DOFs of gear and pinion, respectively |
| $\varphi_1$, $\varphi_2$ | Rotational angles of gear and pinion |
| $\Delta\varphi_2$ | Angle difference between two pairs of gears for the same $\varphi_1$ |
| $\psi_1$, $\psi_2$ | Angle between $OO_2$ and $OA_1$ and the angle between $OO_2$ and $O_2A_2$, respectively |
| $\delta_1$, $\delta_2$ | Acute angle between tangent $t_1$ and $OA_1$ and the acute angle between tangent $t_2$ and $O_2A_2$, respectively |
| $\lambda_1$, $\lambda_2$ | Acute angle between tangent $t_1$ and axis $X_1$ and the acute angle between tangent $t_2$ and axis $X_2$, respectively |
| $\varepsilon_a$ | Tolerable error of the center distance |
| $\mu$, $\sigma$ | Mean and standard deviation of the signal, respectively |

**Acknowledgements** This paper was supported by the National Key R&D Program of China (Grant No. 2018YFB1702400) and the National Natural Science Foundation of China (Grant No. 52075414).

## References

1. Flodin A, Andersson S. Simulation of mild wear in spur gears. Wear, 1997, 207(1−2): 16–23
2. Ding H L. Dynamic wear models for gear systems. Dissertation for the Doctoral Degree. Columbus: The Ohio State University, 2007
3. Tunalioğlu M S, Tuc B. Theoretical and experimental investigation of wear in internal gears. Wear, 2014, 309(1−2): 208–215
4. Wang H B, Zhou C J, Wang H H, Hu B, Liu Z M. A novel contact model for rough surfaces using piecewise linear interpolation and its application in gear wear. Wear, 2021, 476: 203685
5. Wojnarowski J, Onishchenko V. Tooth wear effects on spur gear dynamics. Mechanism and Machine Theory, 2003, 38(2): 161–178
6. Kuang J H, Lin A D. The effect of tooth wear on the vibration spectrum of a spur gear pair. Journal of Vibration and Acoustics, 2001, 123(3): 311–317
7. Wu S J, Zhang H B, Wang X S, Peng Z M, Yang K K, Zhu W L. Influence of the backlash generated by tooth accumulated wear on dynamic behavior of compound planetary gear set. Proceedings of the Institution of Mechanical Engineers. Part C: Journal of Mechanical Engineering Science, 2017, 231(11): 2025–2041
8. Lundvall O, Klarbring A. Prediction of transmission error in spur gears as a consequence of wear. Mechanics of Structures and Machines, 2001, 29(4): 431–449
9. Atanasiu V, Oprisan C, Leohchi D. The effect of tooth wear on the dynamic transmission error of helical gears with smaller number of pinion teeth. Applied Mechanics and Materials, 2014, 657: 649–653
10. Choy F K, Polyshchuk V, Zakrajsek J J, Handschuh R F, Townsend D P. Analysis of the effects of surface pitting and wear on the vibration of a gear transmission system. Tribology International, 1996, 29(1): 77–83
11. Yesilyurt I, Gu F S, Ball A D. Gear tooth stiffness reduction measurement using modal analysis and its use in wear fault severity assessment of spur gears. NDT & E International, 2003, 36(5): 357–372
12. Liu X Z, Yang Y H, Zhang J. Investigation on coupling effects between surface wear and dynamics in a spur gear system. Tribology International, 2016, 101: 383–394
13. Huangfu Y F, Chen K K, Ma H, Li X, Yu X, Zhao B S, Wen B C. Investigation on meshing and dynamic characteristics of spur gears with tip relief under wear fault. Science China Technological Sciences, 2019, 62(11): 1948–1960
14. Huangfu Y F, Zhao Z F, Ma H, Han H Z, Chen K K. Effects of tooth modifications on the dynamic characteristics of thin-rimmed gears under surface wear. Mechanism and Machine Theory, 2020, 150: 103870
15. Brethee K F, Zhen D, Gu F S, Ball A D. Helical gear wear monitoring: modelling and experimental validation. Mechanism and Machine Theory, 2017, 117: 210–229
16. Chen W, Lei Y L, Fu Y, Hou L G. A study of effects of tooth surface wear on time-varying mesh stiffness of external spur gear

considering wear evolution process. Mechanism and Machine Theory, 2021, 155: 104055
17. Chen Z G, Ning J Y, Wang K Y, Zhai W M. An improved dynamic model of spur gear transmission considering coupling effect between gear neighboring teeth. Nonlinear Dynamics, 2021, 106(1): 339–357
18. Chen Z G, Zhou Z W, Zhai W M, Wang K Y. Improved analytical calculation model of spur gear mesh excitations with tooth profile deviations. Mechanism and Machine Theory, 2020, 149: 103838
19. Ding H L, Kahraman A. Interactions between nonlinear spur gear dynamics and surface wear. Journal of Sound and Vibration, 2007, 307(3−5): 662–679
20. Yuksel C, Kahraman A. Dynamic tooth loads of planetary gear sets having tooth profile wear. Mechanism and Machine Theory, 2004, 39(7): 695–715
21. Chin Z Y, Smith W A, Borghesani P, Randall R B, Peng Z X. Absolute transmission error: a simple new tool for assessing gear wear. Mechanical Systems and Signal Processing, 2021, 146: 107070
22. Feng K, Smith W A, Borghesani P, Randall R B, Peng Z X. Use of cyclostationary properties of vibration signals to identify gear wear mechanisms and track wear evolution. Mechanical Systems and Signal Processing, 2021, 150: 107258
23. Feng K, Smith W A, Peng Z X. Use of an improved vibration-based updating methodology for gear wear prediction. Engineering Failure Analysis, 2021, 120: 105066
24. Feng K, Borghesani P, Smith W A, Randall R B, Chin Z Y, Ren J Z, Peng Z X. Vibration-based updating of wear prediction for spur gears. Wear, 2019, 426–427: 1410−1415
25. Amarnath M, Chandramohan S, Seetharaman S. Experimental investigations of surface wear assessment of spur gear teeth. Journal of Vibration and Control, 2012, 18(7): 1009–1024
26. Shen Z X, Qiao B J, Yang L H, Luo W, Chen X F. Evaluating the influence of tooth surface wear on TVMS of planetary gear set. Mechanism and Machine Theory, 2019, 136: 206–223
27. Shen Z X, Qiao B J, Yang L H, Luo W, Yang Z B, Chen X F. Fault mechanism and dynamic modeling of planetary gear with gear wear. Mechanism and Machine Theory, 2021, 155: 104098
28. Liang X H, Zuo M J, Pandey M. Analytically evaluating the influence of crack on the mesh stiffness of a planetary gear set. Mechanism and Machine Theory, 2014, 76: 20–38
29. Ma H, Pang X, Feng R J, Song R Z, Wen B C. Fault features analysis of cracked gear considering the effects of the extended tooth contact. Engineering Failure Analysis, 2015, 48: 105–120
30. Huangfu Y F, Chen K K, Ma H, Li X, Han H Z, Zhao Z F. Meshing and dynamic characteristics analysis of spalled gear systems: a theoretical and experimental study. Mechanical Systems and Signal Processing, 2020, 139: 106640
31. Ma H, Li Z W, Feng M J, Feng R J, Wen B C. Time-varying mesh stiffness calculation of spur gears with spalling defect. Engineering Failure Analysis, 2016, 66: 166–176
32. Li Z W, Ma H, Feng M J, Zhu Y P, Wen B C. Meshing characteristics of spur gear pair under different crack types. Engineering Failure Analysis, 2017, 80: 123–140
33. Qin Y, Xiang S, Chai Y, Chen H Z. Macroscopic-microscopic attention in LSTM networks based on fusion features for gear remaining life prediction. IEEE Transactions on Industrial Electronics, 2020, 67(12): 10865–10875